

See discussions, stats, and author profiles for this publication at: <https://www.researchgate.net/publication/318295483>

A Numerical Study on the Thermal Loads During a Supersonic Rocket Retro-Propulsion Maneuver

Conference Paper · July 2017

DOI: 10.2514/6.2017-4878

CITATIONS

3

READS

8,325

5 authors, including:



Tobias Ecker
German Aerospace Center (DLR)

26 PUBLICATIONS 120 CITATIONS

[SEE PROFILE](#)



Etienne Dumont
German Aerospace Center (DLR)

68 PUBLICATIONS 90 CITATIONS

[SEE PROFILE](#)



Sven Stappert
German Aerospace Center (DLR)

26 PUBLICATIONS 60 CITATIONS

[SEE PROFILE](#)

Some of the authors of this publication are also working on these related projects:



VLM Micro launcher [View project](#)



Continuous detonation wave engine [View project](#)

A Numerical Study on the Thermal Loads During a Supersonic Rocket Retro-Propulsion Maneuver

Tobias Ecker* and Sebastian Karl†

*German Aerospace Center (DLR), Institute for Aerodynamics and Flow Technology
Bunsenstr. 10, Göttingen, Germany*

Etienne Dumont‡ and Sven Stappert§

*German Aerospace Center (DLR), Institute of Space Systems
Robert-Hooke Str. 7, Bremen, Germany*

Daniel Krause¶

*German Aerospace Center (DLR), Institute of Composite Structures and Adaptive Systems
Lilienthalplatz 7, Braunschweig, Germany*

Return and vertical landing of the first launch stage is a concept enabling reusable launch systems and has been successfully applied by SpaceX with the Falcon 9. The Falcon 9 first stage descends by two or three phases of retro-propulsion. Especially the supersonic retro-propulsion phase, using three of its nine engines, is of interest as it exhibits conditions close to Mars reentry. During retro-propulsion the first stage is partially submerged in the hot exhaust plume. In this study a generic model based on the Falcon 9's features and dimensions is used to perform a numerical investigation of the plume - vehicle interaction. Using Large eddy simulation (LES) and Reynolds-Averaged-Navier-Stokes equations (RANS) based computational methods the flow field is characterized at different trajectory points during retro-propulsion. Based on several steady RANS calculations, an aerothermal database is created and coupled into a simple finite element structural heating model of the casing. Results show, that despite the high gas temperatures, the low gas density leads to a manageable heat flux and only moderate temperature increase on the cylindrical walls when using conventional Aluminum materials.

Nomenclature

Roman symbols

h	altitude	T	thrust
I_{sp}	specific impulse	u	streamwise velocity
r	radius	w	wall thickness
Re	unity Reynolds number	x, y, z	coordinates
\dot{m}	mass flow rate	X	mole fraction
M	Mach number	Y	mass fraction
q	heat flux		
t	time	α	angle of attack
T	temperature	ρ	density

Subscript

w	wall
max	maximum value
vac	vacuum condition
∞	freestream condition
0	total condition

Greek symbols

*Research engineer, Spacecraft Department, AIAA Senior Member

†Research engineer, Spacecraft Department

‡Research engineer, Department Space Launcher Systems Analysis (SART)

§Research engineer, Department Space Launcher Systems Analysis (SART)

¶Research engineer, Structural Mechanics Department

I. Introduction

Reusable launch systems have been proposed multiple times throughout history of space flight and resulted in several partially reusable systems (e.g. Space Shuttle). Most recently, private companies like SpaceX and Blue Origin have successfully demonstrated an important first step in the re-usability of commercial launch systems with the return and vertical landing of the first launcher stage and its reuse in a subsequent launch. The SpaceX Falcon 9 first stage typically descends by two to three phases of retro-propulsion. Especially the supersonic retro-propulsion phase is of interest as it exhibits conditions close to Mars reentry. During this retro-propulsion phase the first stage flies through its own hot exhaust plume created by three of its Merlin 1D+ engines. NASA thermal imaging of the Falcon 9 return maneuver shows the rocket casing to be partially submerged in an strongly in-stationary envelope of hot gases during retro-propulsion. This study aims to investigate the heating of the casing during supersonic retro-propulsion by coupling the aerothermal loads with a simple structural heating model.

In a first step, a system analysis of the staging and the structural composition of the Falcon 9 vehicle is performed based on the information released by SpaceX. The model of Falcon 9 FT has been improved incrementally based on the modeling of the previous versions on Falcon 9.¹⁻⁴ The resulting system and the applied tools were validated using trajectory data from Falcon 9 missions and is confirmed to be representing the Falcon 9 Full Thrust (FT) ascent, descend and return capabilities. Using these boundary conditions, a numerical study on the thermal loads on the casing wall during the Falcon 9 supersonic retro-propulsion maneuver for the Orbcomm OG2 mission profile was carried out. Both Large eddy simulation (LES) and steady Reynolds-Averaged-Navier-Stokes equations (RANS) computational approaches are investigated for studying the unsteady rocket plume flow field at a critical point on the return trajectory. Successively, a multitude of RANS calculations at a number of trajectory points during retro-propulsion were carried out and analyzed with regards to plume extension, plume-drag interaction and heat flux distribution. Based on this data, an aerothermal database was built and used in conjunction with a finite element model of the wall casing in order to estimate the casing wall temperature during retro-propulsion for several wall thicknesses.

II. Launcher system overview

Falcon 9 FT (Full Thrust) is a two stage to orbit launch vehicle (TSTO). The stages are propelled by the Merlin 1 D+ engine, which is a gas generator, open-cycle and re-ignitable design.⁵ While the first stage relies on 9 Merlin 1 D+ engines with a low expansion ratio nozzle, the upper stage engine is equipped with a high expansion ratio variant of the engine optimized for vacuum conditions. Both stages have a diameter of about 3.66 m and the payload fairing has a diameter of 5.2 m. The total length of the vehicle, equipped with a fairing is 70.1 m. Falcon 9 utilizes sub-cooled kerosene (RP-1) and sub-cooled liquid oxygen (LOx) as propellant. The sub-cooling has been introduced with the newest version of the Falcon 9 FT, thereby increasing the density of the propellants and leading to a better structural index of the stages (dry mass to propellant mass ratio) and improved performances. Although managing sub-cooled propellant is more challenging, SpaceX has forgone insulation for its stages so far. In order to obtain realistic boundary conditions for the thermal study, a system study on the staging and structure of the Falcon 9 was conducted.⁴

A. First stage

The first stage is about 41.3 m long, the same length as the first stage of the previous version Falcon 9 v1.1. By propellant sub-cooling and displacement of the common bulkhead, it is estimated that at constant tank total volume (approx. 400 m³), the propellant mass has been increased from 386 to 411 metric tons. This is an increase by 6.1 %. A common bulkhead architecture with the LOx tank situated on top of the RP1 tank has been chosen based on public information released by SpaceX. In order to determine the mass of the stages a classic preliminary design study was performed. While the mass of required subsystems is derived from similar subsystems, the structural component masses had to be determined through structural sizing with DLRs software LSAP v0.956. The structural architecture selected by SpaceX is partially known from published pictures. For instance it is known that the RP1 tank of the first stage is stiffened with stringers and frames and crossed by the LOx feed-line. Less information is available on the LOx tank of the current and optimized version of Falcon 9. Consequently the structural architecture of the LOx tank was varied parametrically and resulted in a stringer and frame stiffened structure. The final structure was determined iteratively by estimating the structural mass for different architectures when considering load

cases representing both the ascent and the descent flight loads. These ascent and descent load cases have determined through simulation a posteriori of all Falcon 9 FT launches until May 2016 based on the available flight data. The following eleven load cases have been considered to size the first stage:

Launch/landing pad	Ascent	Descent
<ul style="list-style-type: none"> • Launcher empty on the launch pad and under wind loads • Launcher fueled but not pressurized and under wind loads • Launcher fueled and pressurized on the launch pad and under wind loads • Rocket (first stage) empty on the barge/landing pad 	<ul style="list-style-type: none"> • During the ascent at maximum product of angle of attack and dynamic pressure (assuming a wind model) • During the ascent at maximum dynamic pressure • During the ascent at maximum acceleration • At first stage jettisoning 	<ul style="list-style-type: none"> • At maximum acceleration during the re-entry boost • At maximum lateral load during the re-entry • At maximum load during the landing burn

Although the temperature of the structure during the descent was assumed to be 150 °C, which is higher than what is computed in section V and therefore leading to poorer material characteristics, it appears that the ascent is still dimensioning the main structures. During the ascent the first stage encounters relatively modest accelerations and dynamic pressures but the propellant loading is high and it is carrying the upper stage and the payload. Additionally, the center of pressure of the vehicle is situated relatively far away from the first stage and therefore the aerodynamic forces are creating high bending moments during the ascent. The resulting structural characteristics of the first stage are given in table 1. Note that the structure described is not necessarily, the one used on Falcon 9. However, it can sustain the loads, encountered by Falcon 9 during its different missions with margins and trajectory analysis with the corresponding structural mass appear to be in agreement with the real flight data. Consequently, it can be concluded that the computed and optimized structure presented is representative of the real Falcon 9 FT structure.

Table 1: Falcon 9 FT, first stage structure as modeled.⁴

Component	Length	Structure type	Skin thickness	Number of stringers	Number of frames
Interstage structure 1/2	6.6 m	Sandwich structure with CFRP skin	3.7 mm	-	-
1st stage LOX tank	22.1 m	Stiffened metallic structure	2.9 mm	90	31
1st stage RP1 tank	14.7 m	Stiffened metallic structure	3.1 mm	116	22
Lower skirt	4.0 m	Sandwich structure with CFRP skin	5.2 mm	-	-

B. Second stage

The second stage is about 9.1 m long, corresponding to a stretch by about 0.9 m from the upper stage of Falcon 9 v1.1. This allows an increase from 97.5 m³ to almost 105 m³ of the tank volume. The larger tank, combined with the propellant sub-cooling, allows the propellant loading to be increased from about 92 tons to over 105 tons. This is an increase by 12.6 %. Just like the first stage, the second stage also has a common bulkhead architecture. According to available data, the LOx tank which is situated on top of the RP1 tank has a monocoque structure whereas the RP1 tank is stiffened with stringers and frames. As in the case of the first stage a structural sizing of the second stage was performed with the load cases corresponding to the flight of the upper stage. The results are summarized in table 2. Once again the resulting structure is not necessarily identical to the real structure of Falcon 9 FT, but it is able to sustain the loads encountered by the second stage of Falcon 9 v1.2 during flight. Further the global mass is such that the trajectory computations match with the demonstrated performance of Falcon 9 FT.

Table 2: Falcon 9 FT, second stage structure as modeled.⁴

Component	Length	Structure type	Skin thickness	Number of stringers	Number of frames
2nd stage LOX tank	5.1 m	monocoque metallic structure	5.0 mm	-	-
2nd stage RP1 tank	4.0 m	Stiffened metallic structure	2.4 mm	116	22

C. Engine performance parameters

The engine used on Falcon 9 FT v1.2 is the Merlin 1D+, this is an evolution of the Merlin 1D used on the Falcon 9 v1.1. The engine is basically the same but the chamber pressure of this gas generator, open cycle engine has been increased from about 97 bar to 108 bar. The mixture ratio is situated between 2.3 and 2.4 for both the first stage and the upper stage version of the engine. The main change from the Merlin 1D is the mass flow rate which as now increased to about 272 kg/s, including about 22.77 kg/s through the gas generator. The upper stage engine (Merlin 1D+ vacuum) expansion ratio has been increased from about 117 to 165. This increase may be explained by the higher combustion pressure. It is to note that the inter stage is longer in order to accommodate the larger nozzle on the upper stage engine. The restart capability is obtained by using hypergolic ignition. For this purpose triethylaluminum and triethylborane (TEA-TEB)⁵ are injected into the combustion chamber and ignite when reaction with oxygen occurs. A summary of values from the literature,⁵ online records⁶ and as estimated for this study using DLR's software LRP is given in table 6.

Table 3: Summary of performance parameters Merlin 1D+ based on literature and values as computed with DLR's software LRP.

Parameter	Literature Value ⁵	Literature Value ⁶	Estimated value (LRP)
Thrust (sea level) T	654 kN	723 kN	756 kN
Thrust (vacuum) T_{vac}	716 kN	825 kN	827 kN
Mass flow rate \dot{m}			272 kg/s
Throttle capability	70 - 112 %		
Chamber pressure p_0	108 bar		
Expansion ratio	16		

D. Trajectory

While the trajectories of all missions performed by Falcon 9 until early May 2016 have been computed and optimized, the trajectory of the mission Orbcomm OG2 has been selected for the aerothermal analyses. This is indeed the first mission which demonstrated a successful return of Falcon 9 first stage, the first mission of Falcon 9 FT and therefore the first flight for which data were available. The maiden flight of Falcon 9 FT took place on December 22nd, 2015 from Cape Canaveral Air Force Station Launch Complex 40. For this first mission it should launch eleven Orbcomm OG2 telecommunication satellites. Each OG2 satellite has a mass of 172 kg, giving a total payload mass without dispenser of 1892 kg. Falcon 9 FT launched them directly in a 620 km x 660 km, 47°orbit. After separation of the first stage the second stage ignited to inject the satellite on the target orbit. Simultaneously, the first stage performed a return flight to the launch site. After performing three engine boosts the first stage landed smoothly on Cape Canaveral Air Force Station Launch Complex 13, also called Landing Zone 1 by Space X. Each of the three boosts has a particular purpose.

1. The boost back burn aims at inverting the horizontal velocity and redirecting the first stage towards the landing area. It is performed with three engines.
2. The re-entry boost decelerates the stage before it reaches the denser layers of the atmosphere. It is also performed with three engines. This boost is particularly interesting from an aero-thermodynamic point of view and is the subject of the analysis of the following section IV.
3. The landing boost enables landing on the landing pad. It is performed only using the central engine, which is also throttled down at the end of this phase to allow a smoother landing.

With the help of the data from the launch webcast and the technical characteristics of the launcher, it was possible to model iteratively the whole launcher trajectory as seen in figure 1. The trajectory used to perform the aerothermodynamic analysis of the retro boost has been determined with the DLR in-house tool *tosca* in the version 1.221, which used a Runge-Kutta 4/5 integration method. The goal of the optimization was to minimize the required propellant mass and therefore limit the impact of the Return to Launch Site (RTLS) on the launcher performance. Limits in term of maximum dynamic pressure were set, but not reached in the case of this mission. The optimized trajectory differs slightly from the trajectory used for the analyses presented in this paper^a. However it has to be noted that for each of the missions which included a return of the first stage to the launch complex or a landing on the barge, a different descent trajectory has been used leading to a relatively large domain of applicable Re and Mach numbers during supersonic retro-propulsion.

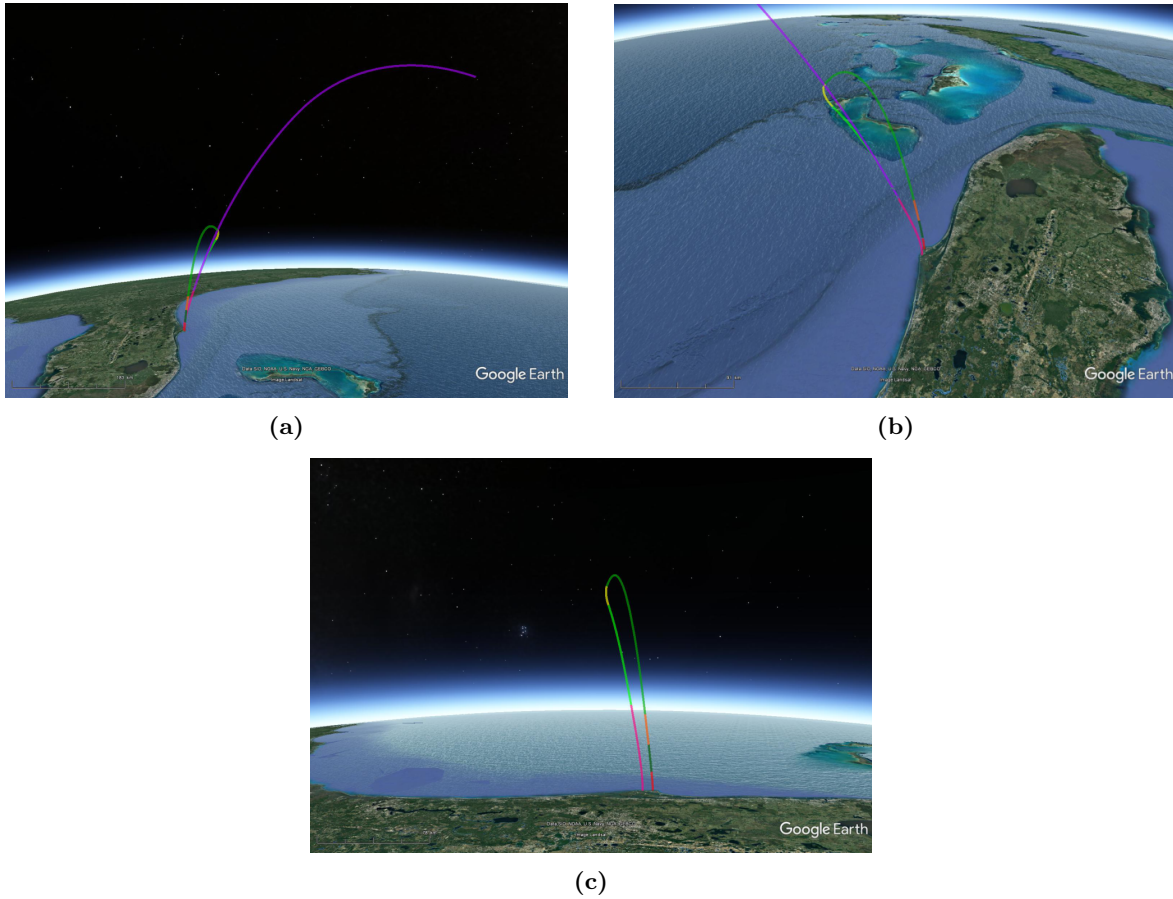


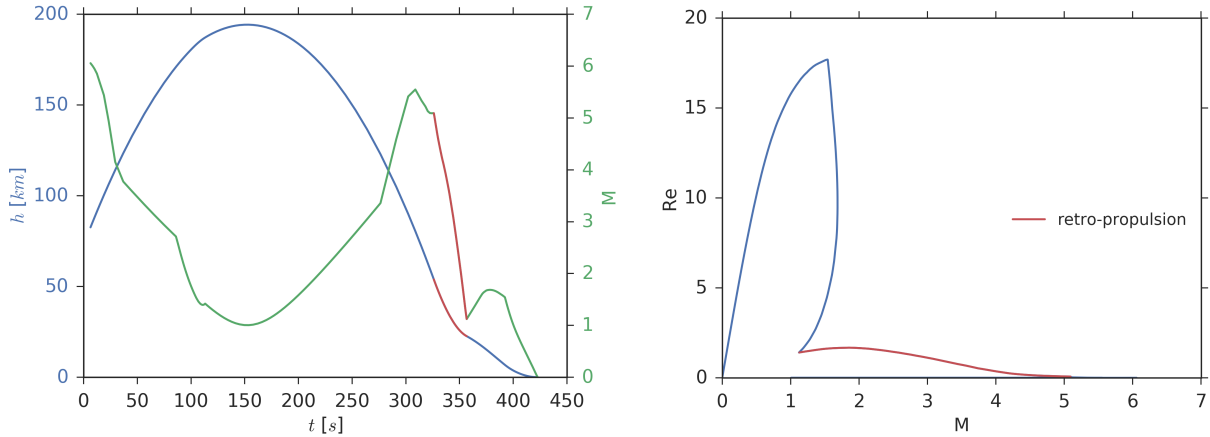
Figure 1: Estimated launcher trajectory. The propelled ascent of the first stage is plotted in dark pink, the ascent of the second stage is plotted in violet, the first ballistic phase is shown in light green, it is followed by the boost back burn in yellow and the second ballistic phase in green. The re-entry burn (subject of this study) is shown in orange, the third ballistic stage in dark green and the landing burn is displayed in red. (Map material: Google Earth, SIO, NOAA, US Navy, NGA, GEBCO, Image Landsat)

Based on the technical model of the launcher presented in the sections A B and C, it has been estimated that almost 53 tons of propellant are required by the first stage to land on the Launch Zone 1, after it has been jettisoned by the second stage. This figure does not include the propellant mass required for the attitude and control maneuvers, such as the 180 flip-over maneuver after the separation of the second stage in preparation of the boost-back burn. The mission specific timeline of the return trajectory of the first stage is shown in table 4 and the evolution of the altitude as a function of the velocity and the time are plotted in Figure 2.

^aIn a later study the descent trajectory has been further optimized with version 1.3 of *tosca* using the SLSQP optimization method and a Runge-Kutta 7/8 integration method.

Table 4: Timeline of the first stage return for the ORBCOMM 2 mission.⁴

Event	Time [s]	Altitude [km]	Velocity [m/s]	Value [-]
MECO	0	72.9	1674.6	
1st burn start	85.9	170.9	977.8	
1st burn end	113.2	187.2	510.8	
Apogee	153.7	194.3	361.5	
2nd burn start	326.0	54.0	1664.8	
<i>Maximum acceleration</i>	354.4	23.5	442.7	6.3 g
2nd burn end	356.7	22.6	330.0	
3rd burn start	392.2	6.8	501.7	
<i>Maximum dynamic pressure</i>	392.3	6.8	501.2	73.7 kPa
3rd burn end/landing	422.6	0.004	2.25	



(a) Altitude and Mach number as a function of time after launch. Red indicates supersonic retro-propulsion maneuver.

(b) Reynolds number and Mach number during mission. Red indicates supersonic retro-propulsion maneuver.

Figure 2: Estimated mission profile.

After the separation from the second stage, the first stage performs a relatively long ballistic flight of about 86 seconds. With the increasing altitude the kinetic energy is converted in potential energy and the velocity decreases. Then three engines are ignited to invert the horizontal component of the velocity and redirect the rocket stage towards the landing zone. This phase lasts for about 27.3 s and finishes before reaching the apogee at more than 190 km. Note that this high altitude is explained by the relatively small pitch over maneuver performed at the beginning of the ascent. It allows reducing the amount of propellant required for the boost back maneuver. But it has a negative impact on the performances for the ascent. In the case of the Orbcomm OG2 mission, the mass to be put into orbit was relatively modest compared to the performance of the launcher and flying a less optimal ascent trajectory was consequently not problematic. The first stage then starts descending towards the landing zone. At an altitude of about 54 km three engines are re-ignited for the re-entry burn. The velocity is decreased from about 1660 m/s to 330 m/s. At engine cut-off the altitude is just above 22 km and the acceleration has reached the maximum value for the return maneuver. During this phase, the stage is already very light, and the loads on the structure are limited. The landing boost, with one engine, starts about 35 s later. During this boost the maximum dynamic pressure is reached. The engine is rapidly throttled down close to the ground and 7 minutes after the separation with second stage, the first stage lands on the Landing Zone 1. After the landing, the first stage displayed soot on its surface, probably coming from the combustion of the propellant. It appeared to be in a relatively good shape, even if it is not possible to tell based on the published data, what effort would be required to refurbish the vehicle for a new flight. This flight was a stepping stone for achieving the reusability of launcher first stage and could bring large advantages in term of cost and flexibility. Reusability is however coming with a cost. According to the analyses performed on the trajectory, Falcon 9 FT could have launched up to about

4.6 tons. The completely expandable version of the vehicle could have launched more than 13 tons on the same target trajectory. In this case the return of the first stage is coming with a loss of almost 65% in term of payload performance.

III. Methodology

In this section the methodology, domain geometry and boundary conditions of the numerical analysis based on computational fluid dynamics (CFD) computations is detailed. Further the engine model based on the performance data which was estimated in the previous section and used for the trajectory analysis is described.

A. Numerical model

All numerical investigations in the framework of the present study were performed with the hybrid structured/unstructured DLR-Navier-Stokes solver TAU,⁷ which is validated for a wide range of steady and unsteady sub-, trans- and hypersonic flow cases. The TAU code is a second order finite-volume solver for the Euler and Navier-Stokes equations in the integral form using eddy-viscosity (RANS), Reynolds-stress or detached- and large eddy simulation (LES) for turbulence modeling. For the steady RANS investigations, the Spalart-Allmaras one-equation eddy viscosity model⁸ was used. The unsteady computations use the same turbulence model operated in LES mode through a modified length scale and a Jameson-type dual time stepping approach⁹ for temporal discretization. The AUSMDV flux vector splitting scheme was applied together with MUSCL gradient reconstruction to achieve second order spatial accuracy. The applied model for thermodynamic and transport properties is based on a non-reacting mixture of two thermally perfect gases (air and engine exhaust gas).

B. Geometry and boundary conditions

The simplified Falcon 9 geometry is represented by a generic cylinder with a symmetrical nine engine configuration at the base. SpaceX calls this octagonal distribution around one center engine a *octaweb* configuration. The engine nozzle contour, which was also used to determine the engine model flow, is based on photographs of the Merlin 1D+ engine. The radius of the diverging contour is modeled from a 2 order polynomial $r(x) = Ax^2 + Bx + C$ (in [m]), with the coefficients being: -0.187051, 0.532439, 0.119. During the supersonic reentry maneuver only three of the nine engines are used. For the purpose of the presented studies the nozzle outflow conditions are imposed onto the active engines as a Dirichlet boundary condition and the excess mass flow of the gas generator exhaust is neglected.

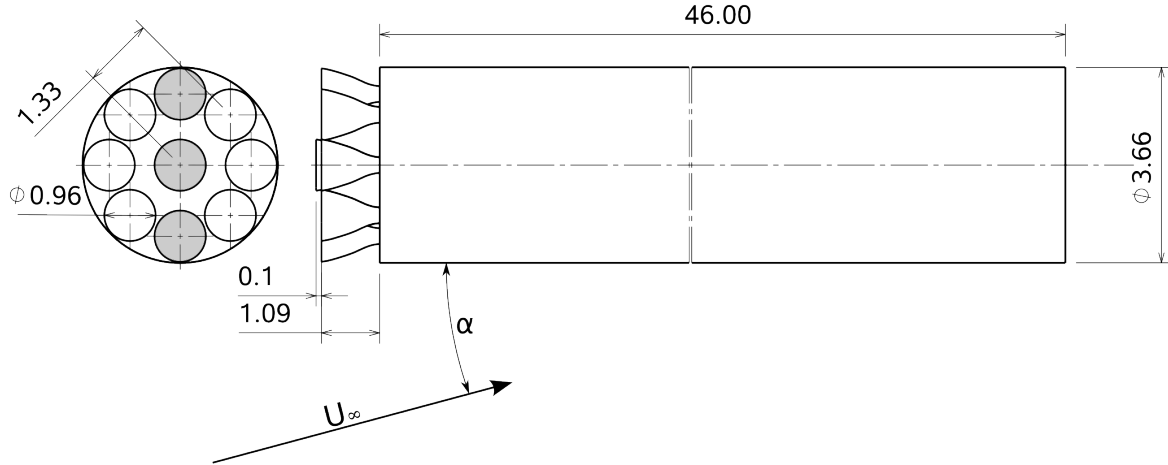


Figure 3: Simplified geometry of Falcon 9 first stage with octaweb engine configuration. Only engines on X-Z plane (marked grey) are used for retropropulsion maneuver. All dimensions in [m].

C. Engine model

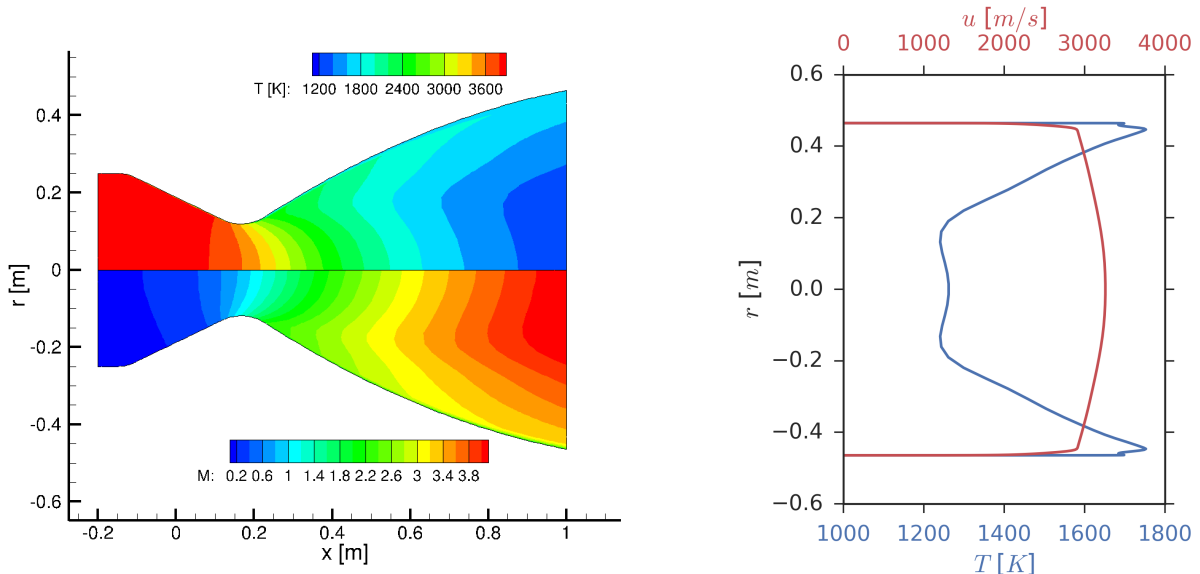
The Merlin 1D+ engine exhaust flow was modeled as an 2D axisymmetric converging-diverging contoured nozzle flow. The exhaust gas composition at the throat was estimated by using NASA CEA¹⁰ for the given

engine pressure and then modeled as a thermally perfect and frozen gas. The exhaust gas composition can be found in table 5. The plenum temperature was then varied to set the engine mass flow rate to be close to the real engine values.

Table 5: Exhaust gas composition of engine model.

Species	Y	Species	Y
CO	3.9547e-1	H ₂	1.5024e-1
CO ₂	9.7310e-2	H ₂ O	3.0706e-1
COOH	1.7644e-5	O	1.9350e-3
H	2.2984e-2	OH	2.3384e-2
HCO	4.7436e-5	O ₂	1.5200e-3
HO ₂	1.3580e-5		

The exhaust nozzle internal flow was modeled using TAU's steady state RANS solver and the Standard Spalart Allmaras turbulence model. The internal velocity contour as well as the exit profile of temperature and velocity are displayed in figure 4. In order to match the estimated mass flow rate the plenum temperature had to be set to 3883 K, which is about 10% higher than the CEA flame temperature estimate at this pressure. The wall temperature was set as 1000 K. The specific impulse $I_{sp} = \frac{T}{\dot{m}_g e}$ at this massflow rate matches the expected estimate value of the Merlin 1D+ to about < 1% if the contribution by the gas generator to the thrust are not considered ($\dot{m}_{GG} = 22.77$ kg/s). An overview of the performance parameters compared to estimated values is shown in table 6.



(a) Temperature and Mach number distribution throughout nozzle. (b) Velocity and temperature profile on exit plane.

Figure 4: Engine exhaust nozzle internal flow at $p_0 = 108$ bar and $T_0 = 3883$ K.

Table 6: Engine model parameters. (^a includes thrust from gas generator.)

Parameter	Estimated (LRP)	CFD	CFD/LRP
$\dot{m} - \dot{m}_{GG}$	255.23 kg/s	255.327 kg/s	1.0004
I_{sp}	283.00 s ^a	282.286 s	0.997
$I_{sp vac}$	310.00 s ^a	304.55 s	0.982

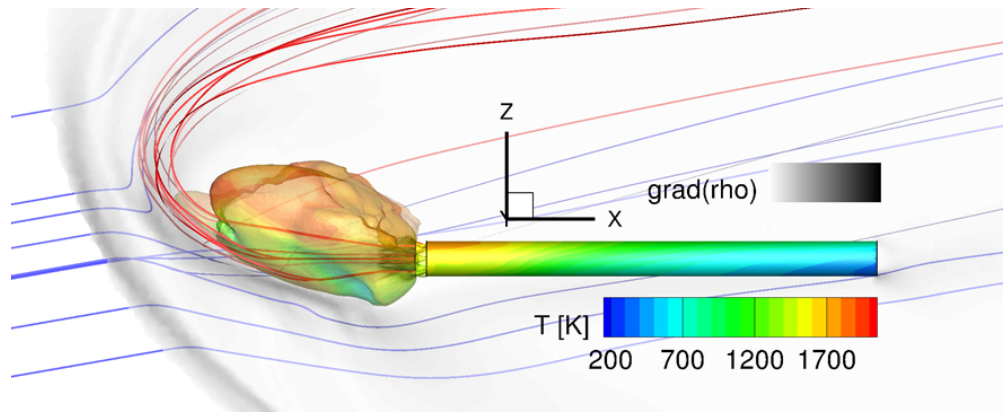
IV. Retro-propulsion plume flow

For this study the retro-propulsion plume flow at a multitude of conditions was modeled. Depending on the trajectory position, the extend of the plume varies drastically, ranging from complete submersion of the vehicle to only partial submersion of the base plate. In order to analyze the required modeling detail, studies using both LES and RANS models were carried out. The geometry and nozzle base flow at the engine exit was described in the previous section. The focus of the main numerical study is on the modeling of the plume during the supersonic retro-propulsion maneuver.

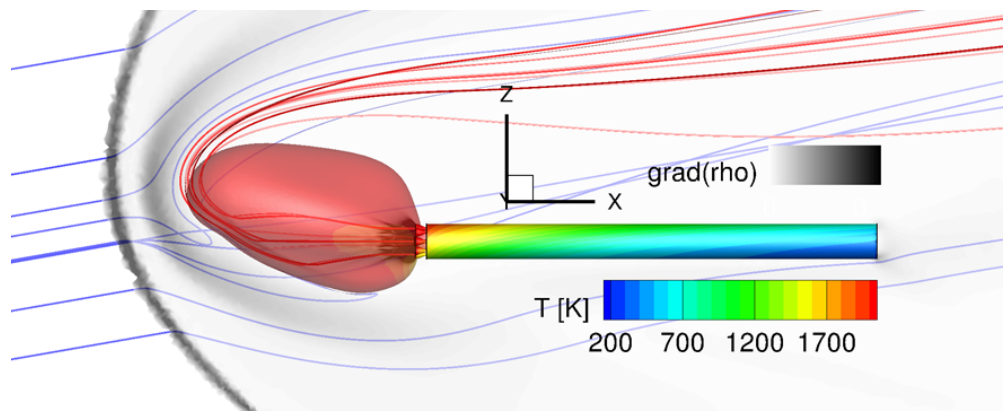
A. Unsteady and steady plume aerodynamics

The flow field during the retro maneuver is characterized by significant unsteadiness of the engine plume. The establishment of an aerothermodynamic database for the analysis of the heating process of the first stage structure requires a large number of computations and was, therefore, based on RANS computations. To assess the accuracy of a steady state RANS result for the present flow conditions, an unsteady computation was carried out for the most critical part of the trajectory (Mach 2 at an altitude of 25km). LES turbulence modeling as described in section III A was used.

A comparison of the plume structure between the averaged LES flow field and the corresponding RANS result is shown in figure 5. Both results show a large detached shock wave upstream of the vehicle and its exhaust plume. The shock wave transitions into an oblique shock at larger distances from the vehicle main axis. The averaged LES results show the shock location to be varying due to the unsteadiness of the plume. In general, the flow field appears to be similar, however, significant differences in the temperature of the exhaust gases are observed.



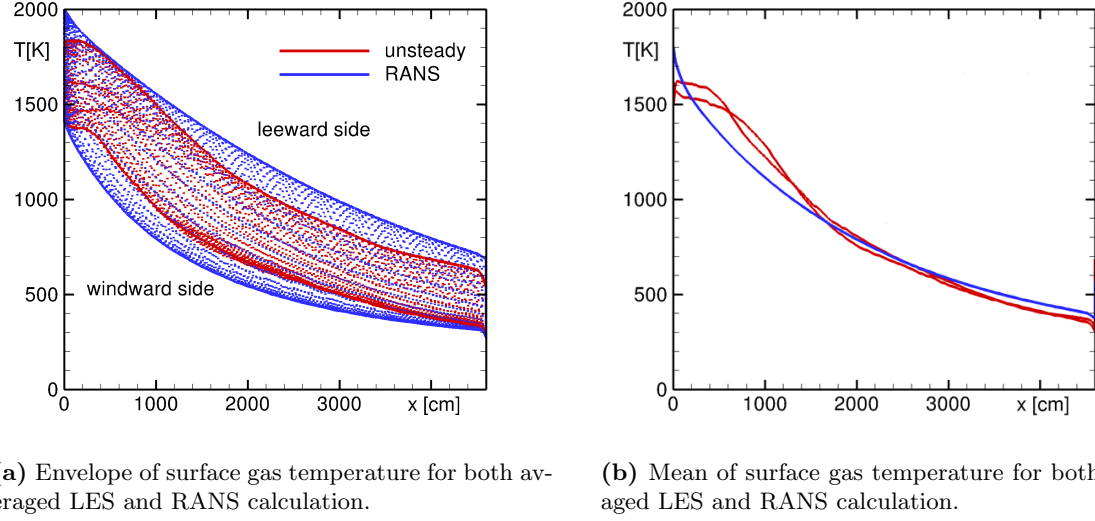
(a) Averaged LES flow field, plume is shown as iso-surface at 50 % exhaust gas mass fraction. Rocket casing contour shows gas temperature.



(b) RANS flow field, plume is shown as iso-surface at 50 % exhaust gas mass fraction. Rocket casing contour shows gas temperature.

Figure 5: Comparison of averaged LES and RANS flow field at $\alpha = 10^\circ$, $h = 25$ km, $M_\infty = 2$.

The gas temperatures close to the vehicle surface are compared in figure 6 on both the windward and leeward side for both numerical approaches. While the range of temperatures predicted by the steady RANS solution is larger when compared to the unsteady LES solution, the RANS modeling is capable to sufficiently predict the average flow properties in the close vicinity of the vehicle (compare figure 6b).



(a) Envelope of surface gas temperature for both averaged LES and RANS calculation.

(b) Mean of surface gas temperature for both averaged LES and RANS calculation.

Figure 6: Comparison of averaged LES and RANS surface gas temperature at $\alpha = 10^\circ$, $h = 25$ km, $M_\infty = 2$.

B. Plume - drag interaction

In order to quantify the interaction between the hot exhaust plume and the body drag during the retro-propulsion phase, selected cases with engine *on* and *off* were simulated using the RANS procedure. The previously introduced case of the first stage returning at an angle attack of $\alpha = 10^\circ$ for engine *on/off* is shown in figure 7. Turning off the engine leads to a reduction of the stand off distance between the detached shock wave and the rocket structure, as well as reduction of the dimensions of the normal shock itself. The expansion wave following on the upper side of the structure does not exist with engines active due to the large exhaust plume. Several cases at zero angle of attack and 10° angle of attack were considered for investigating the effect of the plume on the drag. An overview of the case properties and the resulting drag and lift coefficients is given in table 7.

Table 7: Comparison of drag and lift with and without engine.

Case	A1	A2	B1	B2	C1
α [$^\circ$]	0	0	10	10	0
h [km]	25	25	25	25	40
engine	off	on	off	on	off
c_d	1.56	32.0	1.75	31.8	1.61
c_l	0	0	0.463	-5.34	0
c_d (no engine)		-0.05		0.135	
c_l (no engine)				0.235	

As expected the activation of the engines provides a significant contribution to the force opposing the main motion of the rocket. In consequence this leads to very high drag coefficients for both zero and 10° angle of attack cases. While the the existence of the exhaust plume leads to a lower (case B2) or even negative aerodynamic drag (case A2), the additional thrust provided by the engines establishes drag coefficients higher by an order of magnitude. The difference in drag coefficient (without considering the influence of the

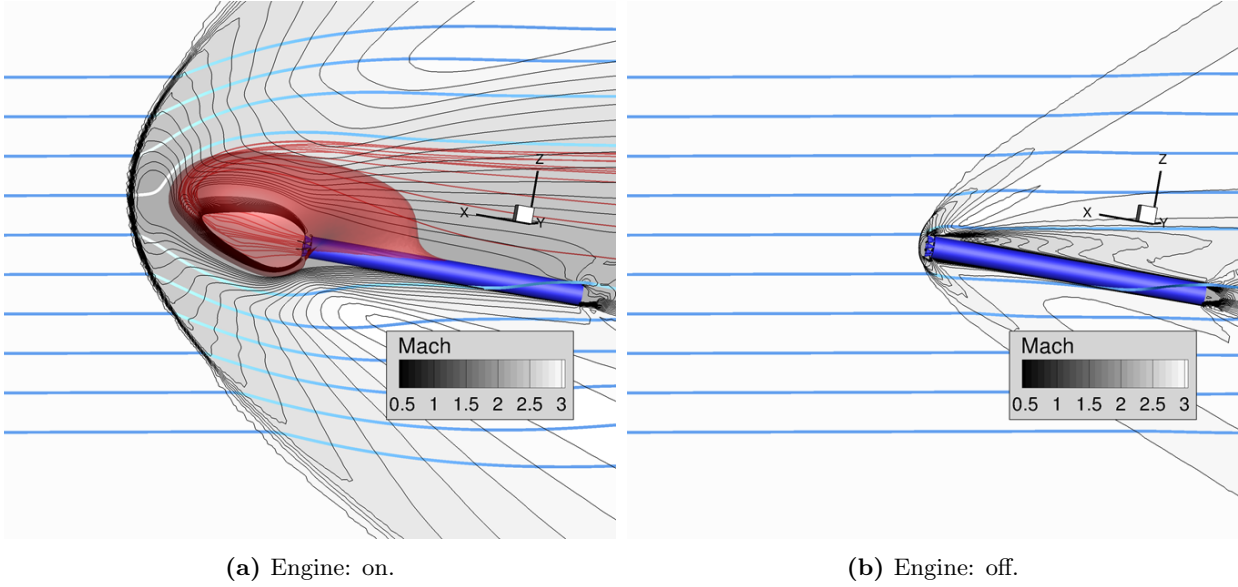


Figure 7: Comparison of flow field with engine off and engine on configuration at $\alpha = 10^\circ$, $h = 25$ km, $M_\infty = 2$.

thrust) are caused by a trade off between lower skin friction drag due to the low density exhaust plume and the effects of flow reversal, as well as the decrease in pressure in front of the vehicle caused by the plume. As the existence of the plume directly influences the pressure drag, the total drag and the aerodynamic drag cannot be completely separated. In the case of the 10° angle of attack the additional transverse thrust component causes a shift of the lift coefficient from a slightly positive value (B1) to a negative value (B2), as the transverse thrust vector opposes the lift generated by the rocket body.

C. Plume envelope development on retro-propulsion trajectory

A number of RANS computations covering the entire trajectory of the retro maneuver at an angle of attack $\alpha = 0^\circ$ were carried out. The seven trajectory points which are initially considered are shown in figure 8. Schematics of the flow field structure and plume extension at three different trajectory points are shown in figure 9. The spreading of the plume is considerably reduced as the atmospheric density increases.

The reduced plume spreading induces qualitative changes of the flow field structure as exemplary shown in figure 10 for the trajectory points 1 ($h = 53.8$ km) and 5 ($h = 28.5$ km). At high altitudes, there is attachment of the shear layer between the plume and the air flow at the vehicle surface and a strong back flow close to the engine-side of the first stage. At lower altitudes, the radial extend of the plume is reduced and a more uniform flow establishes around the stage casing.

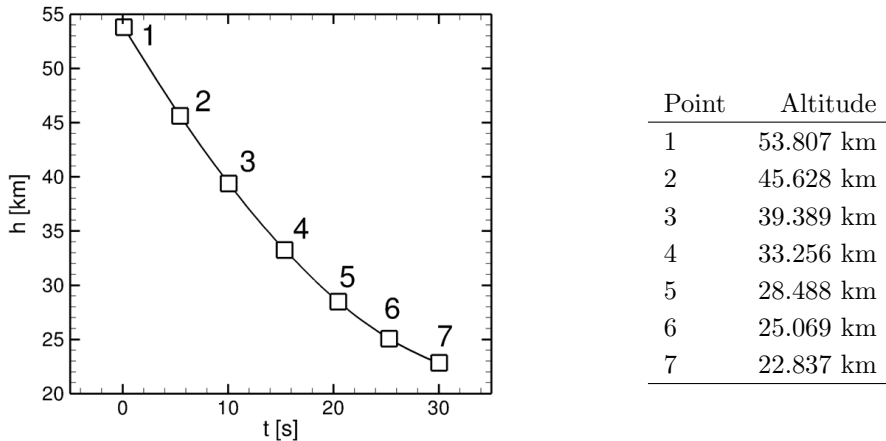
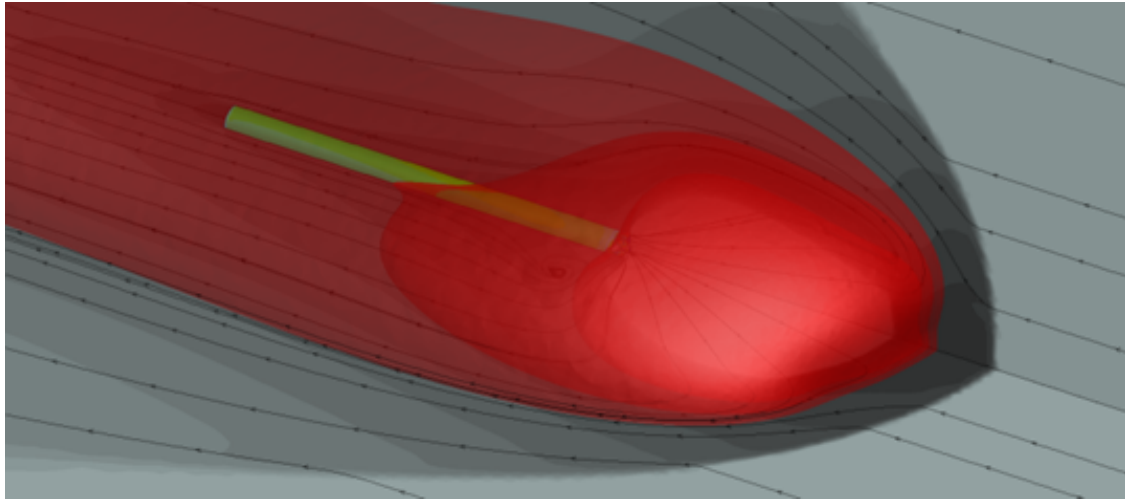
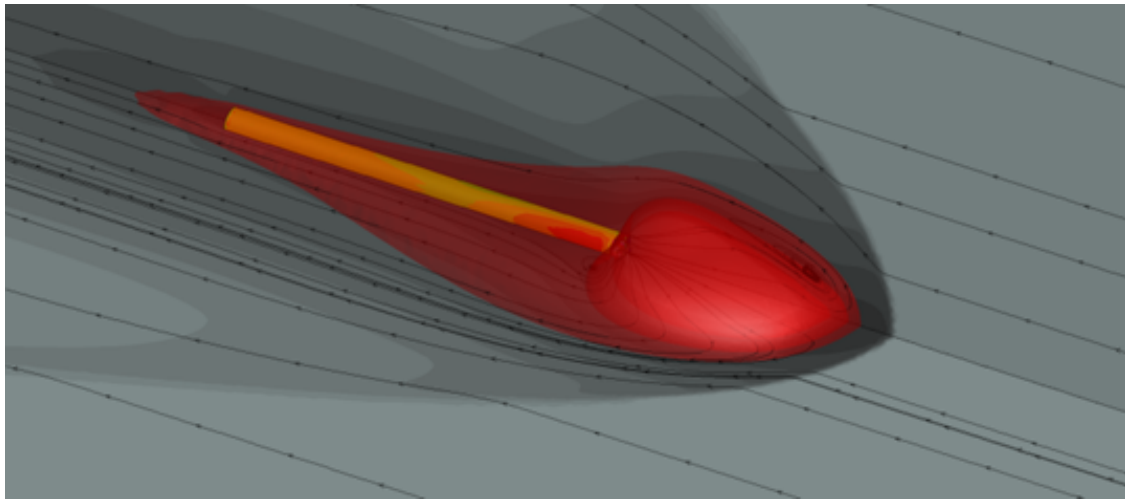


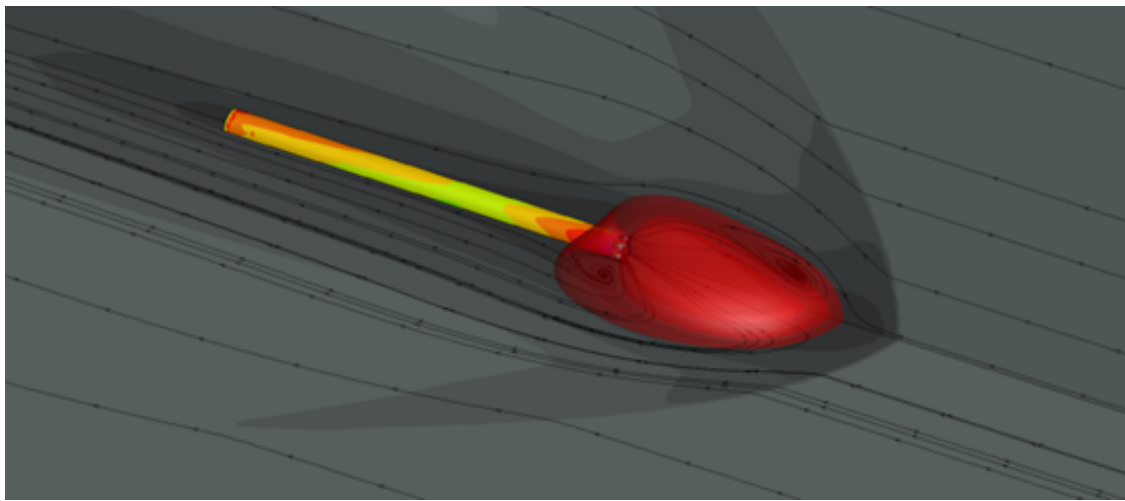
Figure 8: Altitude mach number diagram of retro-propulsion trajectory.



(a) Flow field at trajectory point 2.

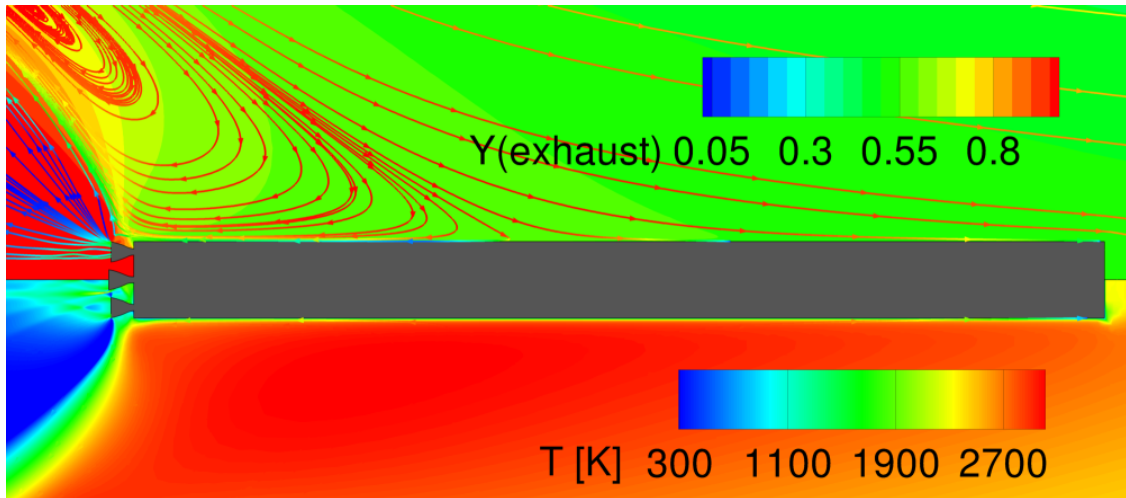


(b) Flow field at trajectory point 4.

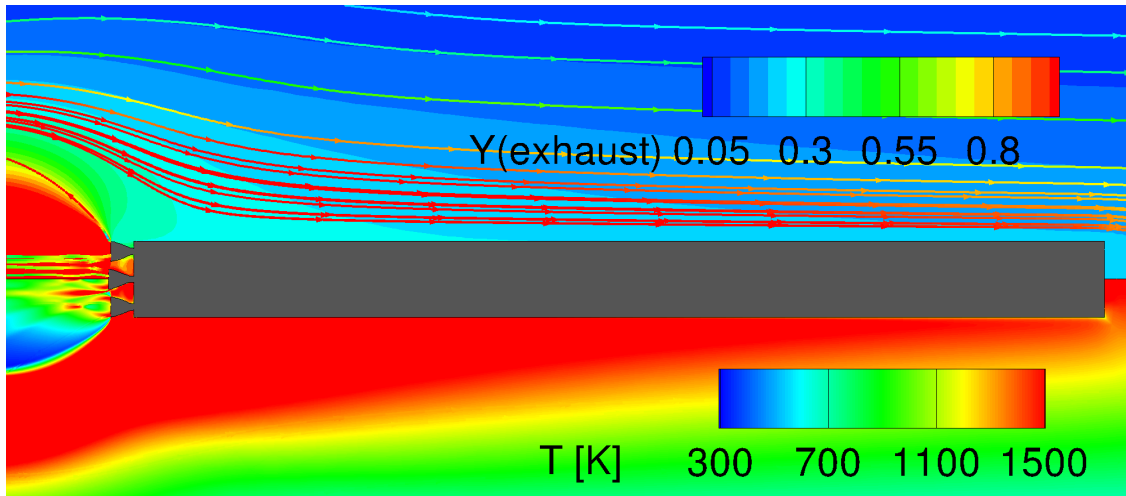


(c) Flow field at trajectory point 6.

Figure 9: Flow fields demonstrating the plume envelope at different trajectory points. Plume envelope defined here as iso-surface at 50 % exhaust gas mass fraction.



(a) Flow field on Z-X plane at trajectory point 1. (top: exhaust gas mass fraction, bottom: gas temperature).



(b) Flow field on Z-X plane at trajectory point 5. (top: exhaust gas mass fraction, bottom: gas temperature).

Figure 10: Exhaust gas mass fraction and gas temperatures at different trajectory points.

V. Aerothermal database

In order to enable modeling of the time-accurate structural heating of the casing during the retro-propulsion maneuver an aerothermal database is necessary. For this purpose RANS calculations of the steady flow field were performed and the wall heat flux determined. In order to decrease the computational effort only an angle of attack α of 0° was considered for this study. As the wall temperature is not known a priori, calculations using different surface temperatures are necessary and result in detailed database containing heat flux as a function of trajectory position and wall temperature. The heat flux profile used for the database was determined on two cut planes of the 45° symmetric geometry denoted as "cold" and "hot side" as shown in figure 11.

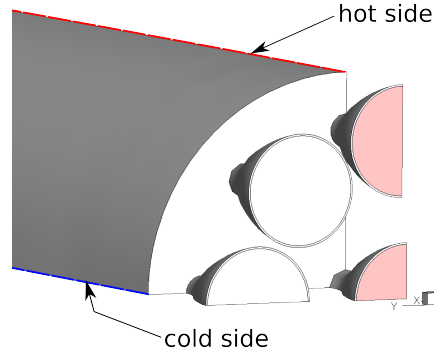


Figure 11: Heat flux evaluation plane nomenclature. "Hot side" denotes the cut plane which is parallel (X-Z) to the 3 engines used for retro-propulsion; the "cold side" denotes the cut plane perpendicular (X-Y) to the active engines (marked in red).

A. Heat flux distribution on casing

The strongly altitude dependent flow field structure must result in qualitative differences of the heat flux distribution. The heat flux distribution at the two evaluation cut planes is shown in figure 12; as expected the cut plane parallel to the three engines used for retro-propulsion (hot side) shows higher heat flux magnitudes towards the base plate at all trajectory points when compared to the perpendicular plane (cold side). For both evaluation planes, the heat flux distribution is strongly dependent on the extension of the plume and therefore on the trajectory position. Hence, a large number of flow field computations are needed to cover these effects and to create an usable aerothermal database.

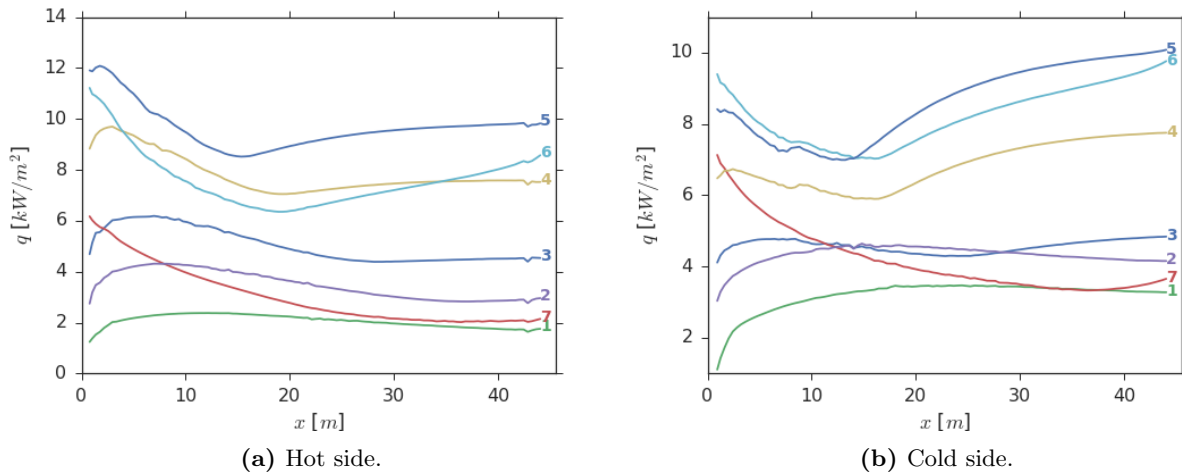


Figure 12: Heat flux at different trajectory points on two evaluation locations ($T_w = 300$ K). Annotated numbers mark trajectory point.

B. Database generation and error estimation

A total of 41 support points at different Re and M numbers, as well as surface temperatures were used to generate the aerothermal database. The majority (28) of these points were directly placed on the trajectory at surface temperatures of $T_w = 300, 400, 500$ and 600 K, while the others were placed in an envelope around the trajectory at positions with strong nonlinear trend. This allows to also generate aerothermal databases for slightly different trajectories (within limits) if needed for optimization processes. An overview of the selected support points is shown in figure 13. The database generation process is detailed in the following paragraph.

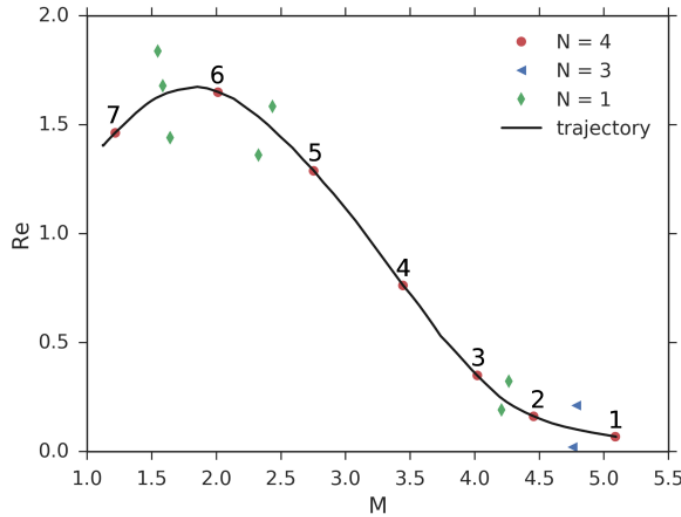


Figure 13: Aerothermal database support points.

Database generation process

1. Extraction of heat flux profiles from CFD surface solution. The heat flux near the edge is limited and kept constant in order to remove unphysical peaks due to modeling limitations at the sharp edges.
2. Grid interpolation of heat flux profile (due to unstructured surface grid).
3. Interpolation of support points for all available surface temperatures ($T_w = 300, 400, 500$ and 600 K) where number of data points $N > 1$. At support points where $N = 1$, the surface temperature influence on the heat flux profile is linearly scaled from the nearest neighbor.
4. Linear interpolation of heat flux profiles for a user defined range of wall temperatures as a function of trajectory flight time from the supporting point matrix (x, Re, M, T_w) via 4D interpolation procedure.
5. Output of database as lookup table for specified trajectory.

The error in the reconstruction was estimated by removing selected support points on the trajectory and reconstructing them from the reduced database. For each investigated trajectory point heat flux data from all available temperature cases at this trajectory point were omitted. The relative RMS error for the 7 main trajectory points is shown in figure 14. As expected, the highest errors are on the start and end point of the trajectory due to the lack of surrounding support points causing an extrapolation scenario - this case is purely hypothetical as the points are contained in the actual database and only removed for reconstruction estimates. All other points have an average RMS reconstruction error between 3.2% and 10 %. Therefore this error estimate can be considered a worst case scenario for interpolation on the trajectory.

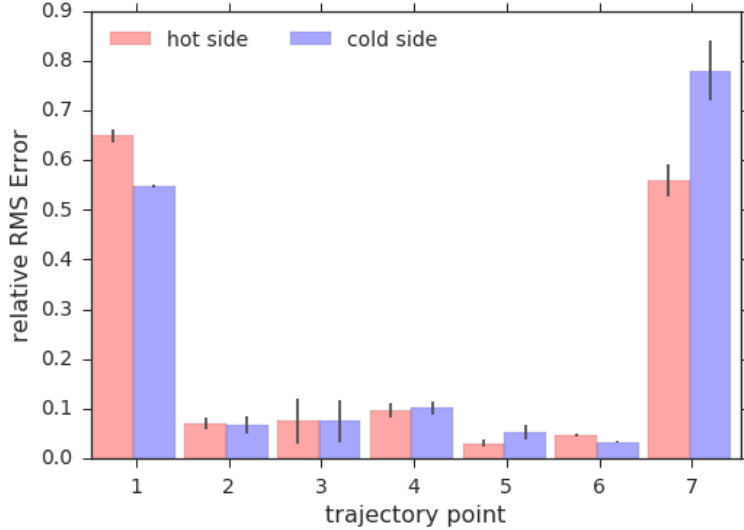


Figure 14: Relative RMS error for heat flux interpolation at support point when only using surrounding support points. Lines indicate standard deviation of RMS error.

C. Aerothermal - structural coupling

A finite element analysis (FEA) is conducted to determine the wall temperature distribution of the stage during the retro-propulsion maneuver. The basis of this analysis is the aerothermal database described previously. Due to different discretization between the database and FEA model the heat flux from the aerothermal database has to be mapped to the structural model first. In a heat transfer analysis, the heat flux is a load while the temperature is the degree of freedom and result variable. However in this analysis, the load (heat flux) depends on the result variable (temperature). Therefore, a time integration has to be performed in which the heat flux load is updated depending on the current temperature as depicted in figure 15.

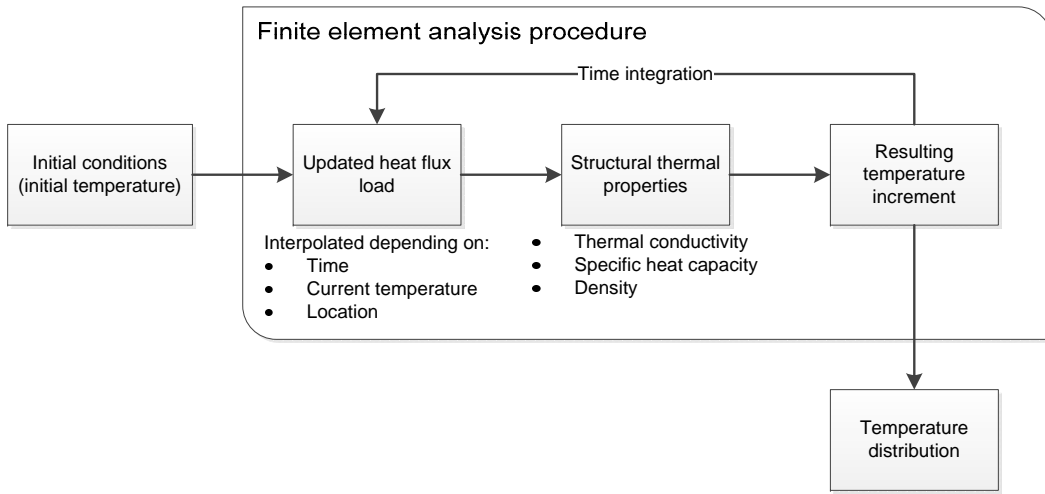


Figure 15: Finite element analysis flowchart.

The analysis is performed with the commercial finite element software package Abaqus. The model assumptions are conservative and should result in a worst case scenario for the wall temperature. Thus, no radiation or heat transfer into adjacent structures are considered for this study. The stage is idealized as a quarter cylindrical shell structure with a radius of 1.8 m without any interior structural elements like domes, stringers or frames, as well as tank contents. The stringers or frames could be taken into account in a smeared manner by increasing the wall thickness accordingly. The structural thermal properties used throughout the analysis are listed in table 8. Since the values of the used Al-Li alloy AA 2198¹¹ are unknown, the properties are generic values based on comparable aluminum alloys.

Table 8: Structural thermal properties used in the analysis.

Property	Value
Thermal conductivity	121 W/(m K)
Specific heat capacity	897 J/(kg K)
Density	2700 kg/m ³

A user-defined heat flux distribution has to be specified in a Fortran subroutine called *DFLUX*. The analysis is a two-step process: In a first run, the coordinates of the integration points are extracted and saved in a separate file. As the aerothermal database currently only contains values for the hot and the cold side, an interpolation of the heat flux values in terms of circumferential angle had to be performed based on the current integration point coordinate. Furthermore, the heat flux values are interpolated in terms of the stage longitudinal axis. Both is performed using a Python script which reads the coordinates of the integration points and interpolates the heat flux values linearly in both angle and length. The interpolated time and temperature dependent heat fluxes for this integration point are then written to file. In the second part of the analysis, these files act as the look up tables provided to the *DFLUX* subroutine. During the analysis, Abaqus calls the subroutine at each integration point at each point in time passing in the current temperature, the time, and the integration point coordinates and expects the heat flux as well as the heat flux derivative with respect to the temperature in return.

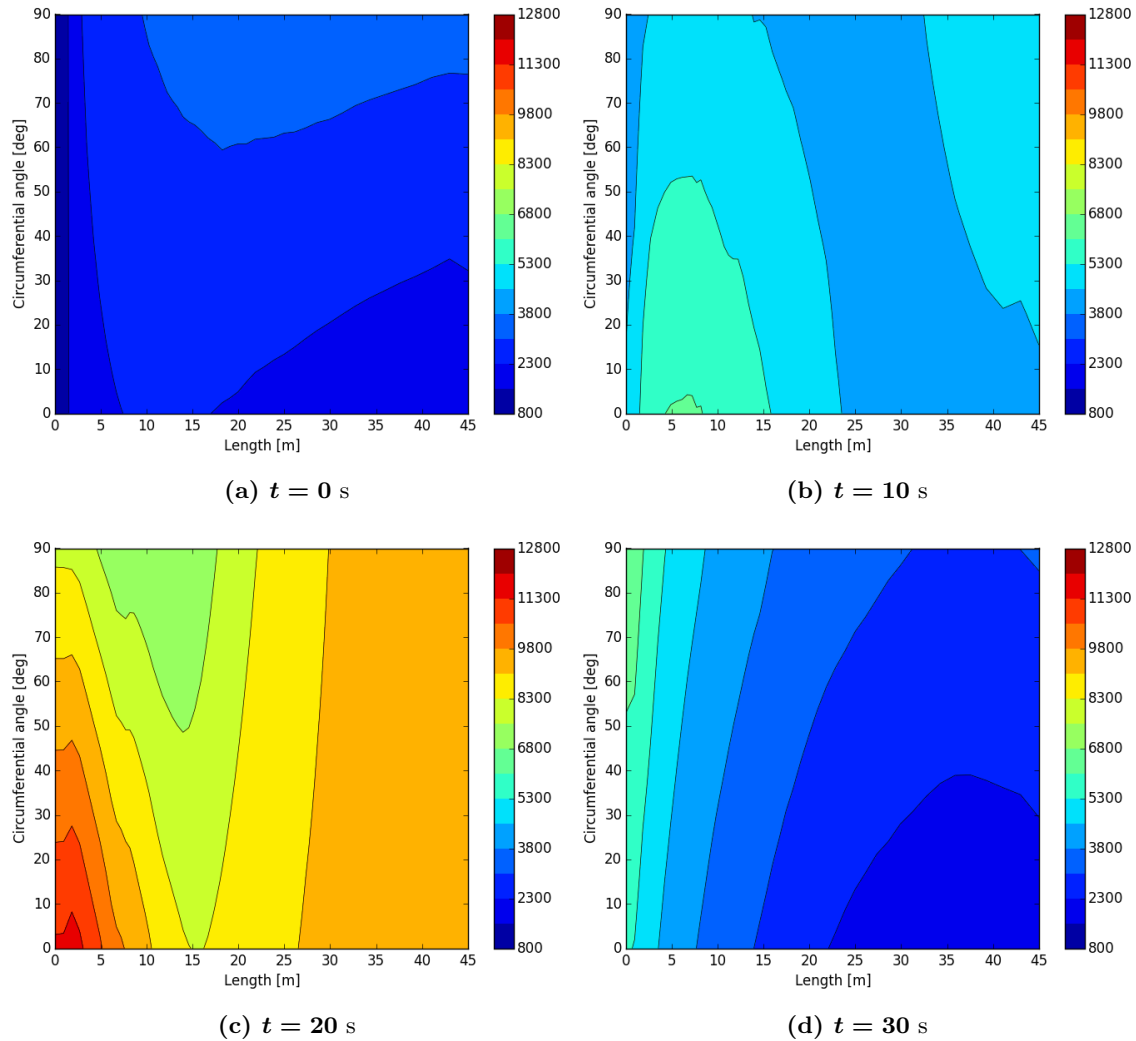


Figure 16: Change of the imposed heat flux (W/m^2) over time for $w = 1 \text{ mm}$.

The analysis has to be initialized which is done using a Predefined Field, i.e. an initial wall temperature distribution. In this case, a constant wall temperature of 300 K is imposed as the initial condition. The resulting heat flux and its change over time is depicted in figure 16 for an assumed wall thickness of 1 mm. Note that the imposed heat flux depends on the wall thickness as a change in thickness changes the resulting temperature and thus the heat flux loading. The heat flux increases and reaches a maximum at $t = 20$ s which correlates to the high Re and low Mach number point in the trajectory (see figure 13).

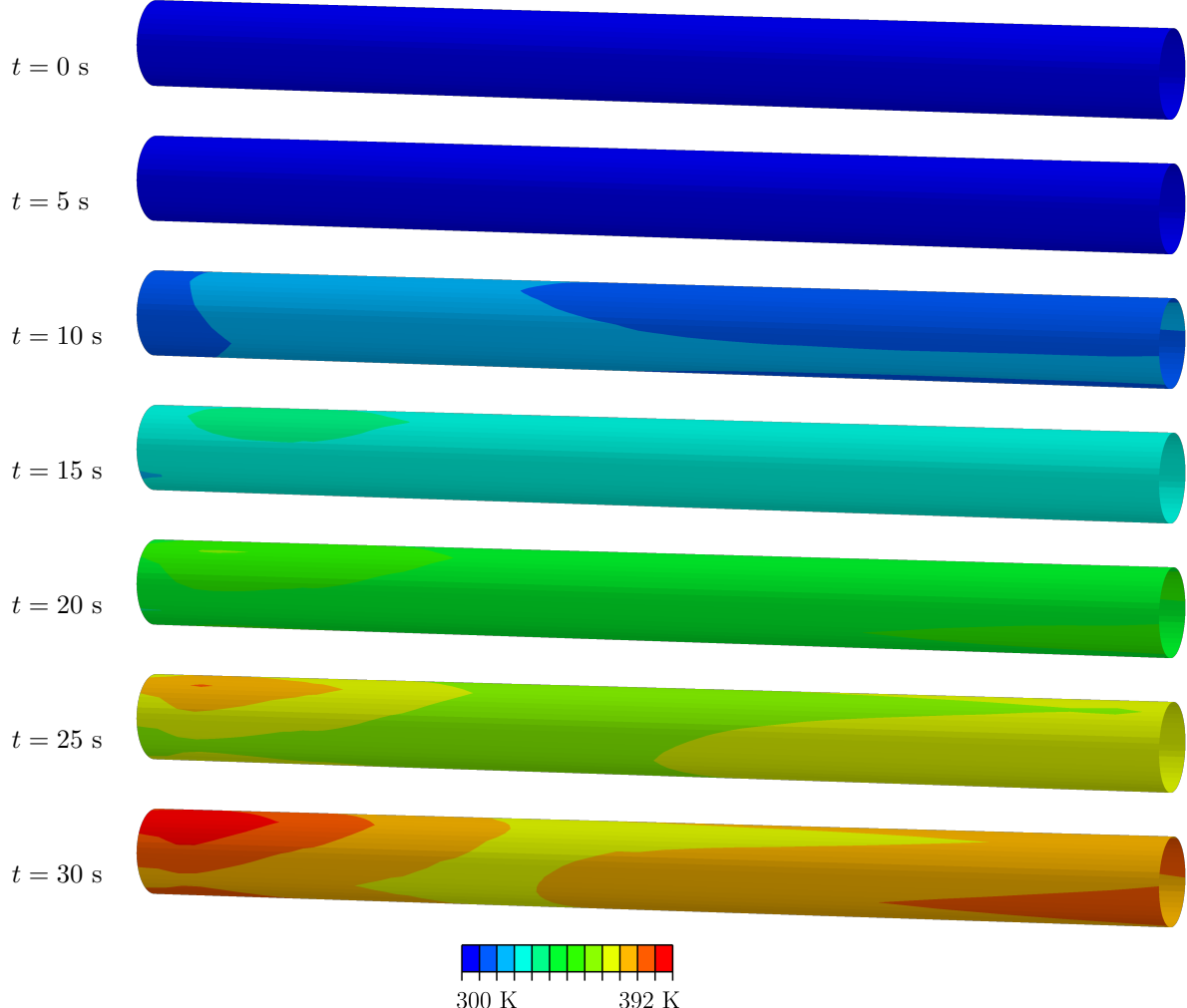


Figure 17: Wall temperature distribution over time during maneuver (quarter model rendered as a full model) for 1 mm wall thickness. The left edge of the rendering corresponds to the aft end of the rocket ($x = 0$ m).

During the start phase of retro-propulsion the casing is completely submerged in the hot exhaust plume which leads to an even heating of the wall structures. With decreasing altitude and Mach number the plume retracts further and further towards the engine side of the rocket (compare figure 9). Combined with the increase in plume density and despite the decrease in surface gas temperature (as can be seen from figure 10) this phenomenon leads to increased wall heat flux and higher wall temperatures close to the aft end. The time dependent development of the wall temperature and final distribution is shown in figure 17 for 1 mm wall thickness. For this case, the maximum temperature increase is 92 K. This seems to be a realistic lower wall thickness considering manufacturing/handling considerations as well as mechanical requirements with respect to strength and stability. Considering the massive idealizations to estimate an upper boundary for the structural heating, a temperature increase of 92 K indicates that the thermal aspect of the retro breaking maneuver is manageable without further thermal protection measures on the side wall.

Considering possible stiffening elements, the thermally effective/smeared wall thickness further increases, thus reducing the maximum temperature even more as shown in table 9 and figure 18. At 3 mm wall

Table 9: Maximum temperature for different wall thicknesses.

Wall thickness	Maximum temperature
1 mm	392 K
2 mm	346 K
3 mm	331 K

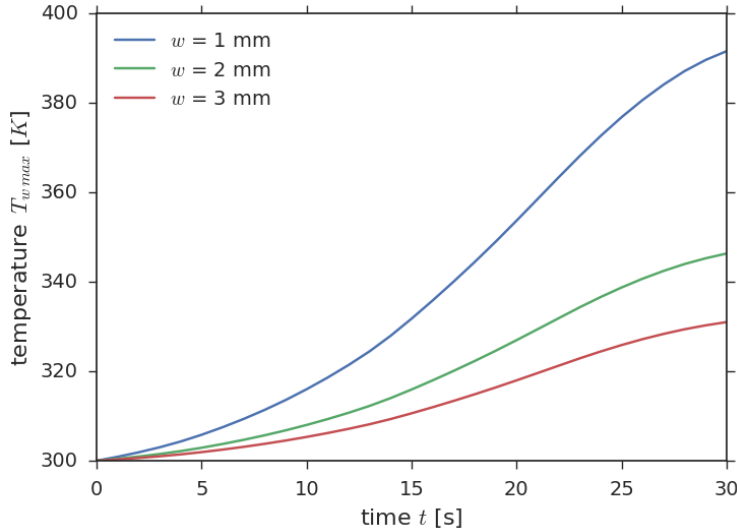


Figure 18: Change of maximum wall temperature over time for selected wall thicknesses.

thickness, the maximum temperature increase is only 31 K still neglecting losses due to radiation and heat conduction into adjacent parts. A sensitivity study reveals that the density has the highest impact on the final temperature distribution. Changing the conductivity (in- and/or out-of-plane) has little impact as the spatial heat flux distribution is relatively uniform at a single point in time. Thus, the temperature differences are small diminishing the impact of the conductivity on the temperature distribution. Two aspects requiring further consideration in future studies are the choice of wall temperature starting distribution, internal structure and tank contents, as well as the influence of motor base plate modeling on the heat flux close to the aft end.

VI. Conclusions

This study aims at studying the plume - vehicle interaction and the resulting thermal loads of the Falcon 9 side walls during supersonic retro-propulsion. For this purpose, a system analysis of the staging and the structural composition of the Falcon 9 vehicle is performed based on the information released by SpaceX. The resulting system is confirmed to be representing the Falcon 9 Full Thrust (FT) ascent, descend and return capabilities.

Several numerical studies of a generic Falcon 9 model during the supersonic retro-propulsion maneuver of the Orbcomm OG2 mission were carried out. First the unsteady rocket plume flow field at an angle of attack of 10° using LES and steady RANS approaches is investigated for one critical point on the trajectory. It is shown that, despite the unsteadiness of the plume, the time averaged LES flow features match reasonably well with predictions based on the steady RANS calculation.

Further, the effect of the exhaust plume on the drag coefficient for different conditions was quantified. As expected the engine thrust provides a significant contribution to the total drag coefficient. Difference in drag coefficients, excluding the engine thrust, are a result of the trade off between skin friction drag and the effects of flow reversal, as well as the decrease in pressure in front of the vehicle caused by the plume. As the plume directly influences the pressure drag, the total drag and the aerodynamic drag cannot be completely separated. Therefore activation of the engine during reentry does not necessarily lead to an intrinsically lower aerodynamic drag.

Successively, RANS calculations at a number of trajectory points during the retro-propulsion maneuver were carried out and the plume extension analyzed. Depending on the trajectory position, the extend of the plume varies drastically, ranging from complete submersion of the vehicle to only partial submersion of the base plate. The influence of the exhaust plume results in very different heat flux distributions on the casing during the maneuver, which need to be determined in order to estimate the structural heating process during retro-propulsion. For this purpose on-trajectory calculations for different temperatures were supplemented by off-trajectory calculations, creating a support point envelope for an aerothermal database. An interpolation process was used to estimate the heat flux on the casing during the maneuver for different wall temperatures. A heuristic analysis of the error of this heat flux estimate resulted in errors below 10 % at relevant trajectory locations.

Time accurate coupling of a simple FEA model of the rocket side wall with the heat flux database allowed to estimate the wall temperatures for several wall thicknesses during the retro-propulsion maneuver. While maximum temperatures are present near the base of the vehicle, the general wall temperature increase for realistic wall thickness is relatively small. Despite the high gas temperatures, the low gas density leads to manageable heat flux on the cylindrical walls when using conventional Aluminum materials without thermal protection. The base plate, which would naturally have thermal protective treatment, was not considered in this analysis as the more complex geometry was not modeled with enough detail for this study.

Acknowledgments

The authors would like to acknowledge funding of this study through the DLR internal project XTRAS managed by Ingrid Dietlein. We also thank Klaus Hannemann for the helpful input he provided in the development of this paper.

References

- ¹Koch, A., Sippel, M., Kopp, A., van Foreest, A. , Ludwig, C., and Schwanekamp,Tobias, “Critical analysis of Falcon 1, 1e, Falcon 9 and Dragon capsule,” Tech. Rep. TN-018/2010, SART, 2010.
- ²Bhagat, M. R., “SpaceX Falcon 9 v1.1, Falcon Heavy remodeling; Falcon 9 v1.1 descent trajectory and performance optimization,” Tech. Rep. TN-020/2014, SART, 2014.
- ³Pouplin, J. and Dumont, E., “Falcon 9 v1.1 and v1.2 performances and first stage descent/return trajectories analyses,” Tech. Rep. TN-009/2015, DLR-IB-RY-HB-2016-5, SART, 2015.
- ⁴Stappert, S. and Dumont, E., “Reusability of launcher vehicles by the method of SpaceX,” Tech. Rep. TN-007/2016, SART, 2016.
- ⁵Seedhouse, E., *SpaceX’s Dragon: America’s Next Generation Spacecraft*, Space Exploration, Springer International Publishing, 4 Nov. 2015.
- ⁶Mueller, T., online: <https://www.quora.com/Is-SpaceXs-Merlin-1Ds-thrust-to-weight-ratio-of-150+-believable>, accessed on 21.11.2016, June 2015.
- ⁷Langer, S., Schwöppe, A., and Kroll, N., “The DLR Flow Solver TAU – Status and Recent Algorithmic Developments,” *AIAA Paper AIAA-2014-0080*, 2014.
- ⁸Spalart, P.R. and Allmaras, S.R., “A One-Equation Turbulence Model for Aerodynamic Flows,” *AIAA Paper AIAA-92-0439*, 1992.
- ⁹Jameson, A., “Time dependent calculations using multigrid, with application to unsteady flows past airfoils and wings,” *AIAA Paper AIAA-91-1596*, 1991.
- ¹⁰Gordon, S. and McBride, B. J., “Computer Program for Calculation of Complex Chemical Equilibrium Compositions and Applications,” Tech. rep., NASA Reference Publication 1311, 1996.
- ¹¹Wanhill, R.J.H., *Aluminum-Lithium Alloys: Chapter 15. Aerospace Applications of Aluminum-Lithium Alloys*, Butterworth-Heinemann, 20 Nov. 2013.